

## CHEMICAL PHYSICS

# A combined molecular dynamics and experimental study of two-step process enabling low-temperature formation of phase-pure $\alpha$ -FAPbI<sub>3</sub>

Paramvir Ahlawat<sup>1</sup>, Alexander Hinderhofer<sup>2</sup>, Essa A. Alharbi<sup>3</sup>, Haizhou Lu<sup>3,4</sup>, Amita Ummadisingu<sup>3</sup>, Haiyang Niu<sup>5,6</sup>, Michele Invernizzi<sup>5,6,7</sup>, Shaik Mohammed Zakeeruddin<sup>3</sup>, M. Ibrahim Dar<sup>3,8</sup>, Frank Schreiber<sup>2\*</sup>, Anders Hagfeldt<sup>4,9\*</sup>, Michael Grätzel<sup>3\*</sup>, Ursula Rothlisberger<sup>1\*</sup>, Michele Parrinello<sup>5,6,7\*</sup>

Copyright © 2021  
The Authors, some  
rights reserved;  
exclusive licensee  
American Association  
for the Advancement  
of Science. No claim to  
original U.S. Government  
Works. Distributed  
under a Creative  
Commons Attribution  
NonCommercial  
License 4.0 (CC BY-NC).

It is well established that the lack of understanding the crystallization process in a two-step sequential deposition has a direct impact on efficiency, stability, and reproducibility of perovskite solar cells. Here, we try to understand the solid-solid phase transition occurring during the two-step sequential deposition of methylammonium lead iodide and formamidinium lead iodide. Using metadynamics, x-ray diffraction, and Raman spectroscopy, we reveal the microscopic details of this process. We find that the formation of perovskite proceeds through intermediate structures and report polymorphs found for methylammonium lead iodide and formamidinium lead iodide. From simulations, we discover a possible crystallization pathway for the highly efficient metastable  $\alpha$  phase of formamidinium lead iodide. Guided by these simulations, we perform experiments that result in the low-temperature crystallization of phase-pure  $\alpha$ -formamidinium lead iodide.

## INTRODUCTION

The perovskite solar cell (PSC) is one of the most promising and cheap photovoltaic technologies (1). However, their widespread application is made difficult by a number of technological problems related to their long-term stability and processability.

Two-step deposition (2) is one of the main experimental techniques used to fabricate highly efficient and stable PSCs (3, 4). In this process, lead iodide (PbI<sub>2</sub>) is first deposited and then converted to perovskite by adding halide salts of monovalent cations such as methylammonium iodide (MAI) and formamidinium iodide (FAI) (5). This process offers several advantages for the industrial-scale fabrication (6–8) of larger modules over the single-step spin-coating technology, which is limited to smaller devices. However, when scaling up, maintaining reproducible high performances and long-term stability is difficult. These problems arise mainly from the lack of control over the fabrication process (9, 10). Therefore, it is essential to understand at the atomic level the mechanism of halide perovskite crystallization.

Among the several perovskites of interest, we study here the two-step fabrication of methylammonium lead iodide (MAPbI<sub>3</sub>) and formamidinium lead iodide (FAPbI<sub>3</sub>). The former is a well-studied system on which many experiments have been performed.

The latter FAPbI<sub>3</sub>, is a compound that, in its  $\alpha$ -FAPbI<sub>3</sub> polymorph, has several attractive features like a  $\sim$ 1.45-eV bandgap, high-charge carrier mobility, and superior thermal stability. The practical application of  $\alpha$ -FAPbI<sub>3</sub> has been hampered by the fact that the  $\alpha$  phase is metastable and that the thermodynamic phase transition requires high temperatures at  $\sim$ 150°C. The main result of this paper is the discovery of a low-temperature pathway to the fabrication of  $\alpha$ -FAPbI<sub>3</sub>. This has been made possible by a combined experimental and theoretical effort that has uncovered the microscopic details of the crystallization process.

Previous experimental research (11–20) on MAPbI<sub>3</sub> has revealed that the two-step process occurs via intercalation of the MA<sup>+</sup> cations in the PbI<sub>2</sub> layers followed by a transformation to the perovskite structure via intermediate phases. However, these experiments could not resolve the nature of intermediate phases nor elucidate the underlying atomistic mechanism. To fill in the details that experiments cannot resolve and obtain an understanding of the microscopic transformation mechanism, we have performed a molecular dynamics (MD) investigation. Because the time scale involved in the fabrication process is too large, we have made use of an enhanced sampling technique. In particular, we have used well-tempered metadynamics (WTMetaD) (21). This method allows simulating processes that take place on an extended time scale with affordable computing resources.

We started by an experimental characterization of MAPbI<sub>3</sub> via Raman scattering. These experiments provided additional evidence that the picture of the initial intercalation followed by a sequence of intermediates states is correct. We then performed WTMetaD simulations and found that transformation from the intercalated initial structure to the final perovskite arrangement takes place via a sequence of intermediates. These theoretical results are in line with present and past experiments (22–26).

The highly satisfactory agreement between theory and experiments in the case of MAPbI<sub>3</sub> encouraged us to theoretically investigate whether a similar process was operational also for the much

<sup>1</sup>Laboratory of Computational Chemistry and Biochemistry, Institute of Chemical Sciences and Engineering, École Polytechnique Fédérale de Lausanne (EPFL), CH-1015 Lausanne, Switzerland. <sup>2</sup>Institut für Angewandte Physik, Universität Tübingen, 72076 Tübingen, Germany. <sup>3</sup>Laboratory of Photonics and Interfaces, Institute of Chemical Sciences and Engineering, EPFL, CH-1015 Lausanne, Switzerland. <sup>4</sup>Laboratory of Photomolecular Science, Institute of Chemical Sciences Engineering, EPFL, CH-1015 Lausanne, Switzerland. <sup>5</sup>Department of Chemistry and Applied Biosciences, ETH Zürich, 8092 Zürich, Switzerland. <sup>6</sup>Facoltà di Informatica, Istituto di Scienze Computazionali, Università della Svizzera italiana, Via G. Buffi 13, 6900 Lugano, Switzerland. <sup>7</sup>Italian Institute of Technology, Via Morego 30, 16163 Genova, Italy. <sup>8</sup>Cavendish Laboratory, Department of Physics, University of Cambridge, CB3 0HE, United Kingdom. <sup>9</sup>Department of Chemistry, Ångström Laboratory, Uppsala University, Box 523, SE-751 20 Uppsala, Sweden.

\*Corresponding author. Email: ursula.rothlisberger@epfl.ch (U.R.); frank.schreiber@uni-tuebingen.de (F.S.); anders.hagfeldt@uu.se (A.H.); michael.gratzel@epfl.ch (M.G.); michele.parrinello@iit.it (M.P.)

less studied  $\alpha$ -FAPbI<sub>3</sub>. This time, we started from simulations and indeed discovered that a two-step process is possible at lower temperatures. This was then followed by a series of in situ x-ray and thin-film experiments that confirmed the outcome of the simulations and enabled the low-temperature formation of phase-pure  $\alpha$ -FAPbI<sub>3</sub> thin films.

## RESULTS

### Raman spectroscopy

We start with the Raman spectroscopy for monitoring the progress of MAPbI<sub>3</sub> formation in the sequential deposition reaction. All the Raman spectra are shown in Fig. 1. The details are discussed in Methods. Now, we take a closer look at the peaks at 140 and 143 cm<sup>-1</sup>, which are associated with the rotational motion of the methylammonium ion in MAPbI<sub>3</sub> (20). We find that intercalation of the MA<sup>+</sup> ions into the lattice causes the appearance of the peak at 140 cm<sup>-1</sup> at early stages of the reaction (Fig. 1B, 15 s), which then shifts toward 143 cm<sup>-1</sup> around 30 s while growing in intensity. The signal disappears and broadens at room temperature, as expected for the perovskite structure (27), as the reaction progresses to completion (see data for 75 s and 6 min). These results are highly consistent with the report by Jain *et al.* (20) who also ascribe these changes to the consumption of PbI<sub>2</sub> and the progress of MAI intercalation. These findings suggest the intercalation of MA<sup>+</sup> into the PbI<sub>2</sub> lattice and the associated structural reorganization that lastly results in the formation of the MAPbI<sub>3</sub> perovskite in the sequential deposition reaction.

### WTMetaD simulations

From the abovementioned experimental findings, we start from the plausible hypothesis that monovalent cations (MA<sup>+</sup>) intercalate between the edge-sharing layers of Pb-I octahedra in PbI<sub>2</sub> (Fig. 2A) and form a quasi-two dimensionally (2D) layered structure, which is similar to the post-perovskite structure (28). We manually construct such a structure by placing MA<sup>+</sup> ions in between the layers of PbI<sub>2</sub> (Fig. 2B). The remaining iodide (I<sup>-</sup>) from MAI is placed on the Pb-I octahedra to have a final charge-neutral layered MAPbI<sub>3</sub> structure. This model is based on experimentally reported intercalated PbI<sub>2</sub> structures (29, 30). We verify the stability of this structure by carrying out a variable cell enthalpic optimization with both classical MD simulations and density functional theory (DFT) calculation. From both techniques, we find that the structure shown in Fig. 2B is stable. Details are presented in Methods. Furthermore, we calculate the powder diffraction pattern of the DFT-relaxed intercalated structure. We find that the first peak of PbI<sub>2</sub> at ~12.7° shifts to ~11.4° for the intercalated structure; see fig. S1. This observation is consistent with the previously reported x-ray diffraction (XRD) experiments on two-step deposition (31).

We proceed with the WTMetaD simulations of the transformation of the intercalated MAPbI<sub>3</sub> to the perovskite. We prepare two different size supercells of the intercalated structure with 32 and 108 formula units of MAPbI<sub>3</sub>, respectively. With these supercells, we perform WTMetaD simulations as outlined in Methods. These simulations are done at different temperatures ranging from 300 to 420 K, corresponding to typical experimental conditions. For both supercells, we successfully observe the transformation of the starting quasi-2D layered intermediate structure to the 3D corner-sharing perovskite (atomistic views of both simulations are shown in movies S1 and

S2). Because we observe a similar transformation mechanism in both cases, we only present the results for the larger supercell, while the results for the smaller system are given in the Supplementary Materials. We find that the phase transition from quasi-2D to 3D perovskite proceeds through distinct intermediary structures as shown in Fig. 2, B to E. This observation can be explained by Ostwald's step rule, which states that metastable structures are formed as intermediate phases before the formation of the thermodynamically stable phase. We also compute the free energy profile to demonstrate the metastability of these intermediates as compared to final perovskite. This is shown in figs. S2 and S3. From these figures and movies, one can see that the intermediate phases are formed by rotating the PbI<sub>6</sub> octahedra over the planes of PbI<sub>2</sub> (along the axis of the Pb-Pb edge-shared octahedra). This is a general pathway to the formation of intermediate structures. In the larger supercell, more PbI<sub>6</sub> octahedra are required to rotate for complete formation of the perovskite structure, which leads to formation of more intermediate phases. We quantify this with the evolution of the first peak ( $q \approx 10 \text{ nm}^{-1}$  corresponding to  $2\theta \approx 14.1^\circ$ ) of the Debye structure factor ( $S_{\text{PbI}_6}$ ) of Pb<sup>2+</sup> ions in cubic perovskites, detailed in Methods. Figure 3 shows the evolution of  $S_{\text{PbI}_6}$  for the larger supercell, while results for the smaller supercell are shown in fig. S4.

Moreover, we further explore the free energy landscape and find a variety of different polymorphic structures. We outline all of the observed phases in fig. S5. By performing variable cell enthalpic optimization with DFT, we find that all of the structures are stable; see the Supplementary Materials. This polymorphic behavior in halide perovskites is related to the existing polytypism in PbI<sub>2</sub> (32, 33), which also gives rise to these intermediates in crystallization. Many of these polymorphs have a high probability of forming during crystallization of other halide perovskite systems, and some of these structures have been already identified experimentally (22–25).

Encouraged by the results for MAPbI<sub>3</sub>, we proceed to study the phase transition of FAPbI<sub>3</sub>. Here, the main practical challenge is to find the possible pathways for crystallization of the pure samples of the photoactive  $\alpha$  phase. We attempt to solve this problem by first performing simulations and then experiments based on insights from the simulations. We carry out simulations similar to the above-reported approach for MAPbI<sub>3</sub>. First, we construct a quasi-2D PbI<sub>2</sub> structure intercalated with FA<sup>+</sup>, similar to the structure in Fig. 2B. We depict this structure in fig. S13B. We perform WTMetaD simulations of two different size supercells of FAPbI<sub>3</sub>; again, as in the case of MAPbI<sub>3</sub>, in both cases, we successfully observe the phase transition to the perovskite structure of FAPbI<sub>3</sub>; see fig. S6. An atomic view of this phase transition is shown in movies S3 and S4. This simulation reveals a direct path (from the intercalated PbI<sub>2</sub>) to the formation of the metastable phase of  $\alpha$ -FAPbI<sub>3</sub> without the need for a high temperature-induced transformation via the  $\delta$  phase. In particular, our findings suggest that  $\alpha$ -FAPbI<sub>3</sub> can be formed at lower temperatures from an initial quasi-2D structure.

### X-ray experiments

Now, we test our simulation results against the experiments. First, we perform ex situ sequential deposition experiments on MAPbI<sub>3</sub> and take XRD measurements at different reaction times; see Methods for details. The XRD spectra of these samples and an unreacted control sample of PbI<sub>2</sub> are shown in fig. S7A. During the initial seconds, we observe a sharpening and narrowing of the (001) peak as the crystallinity of the PbI<sub>2</sub> increases (34–36). As the reaction

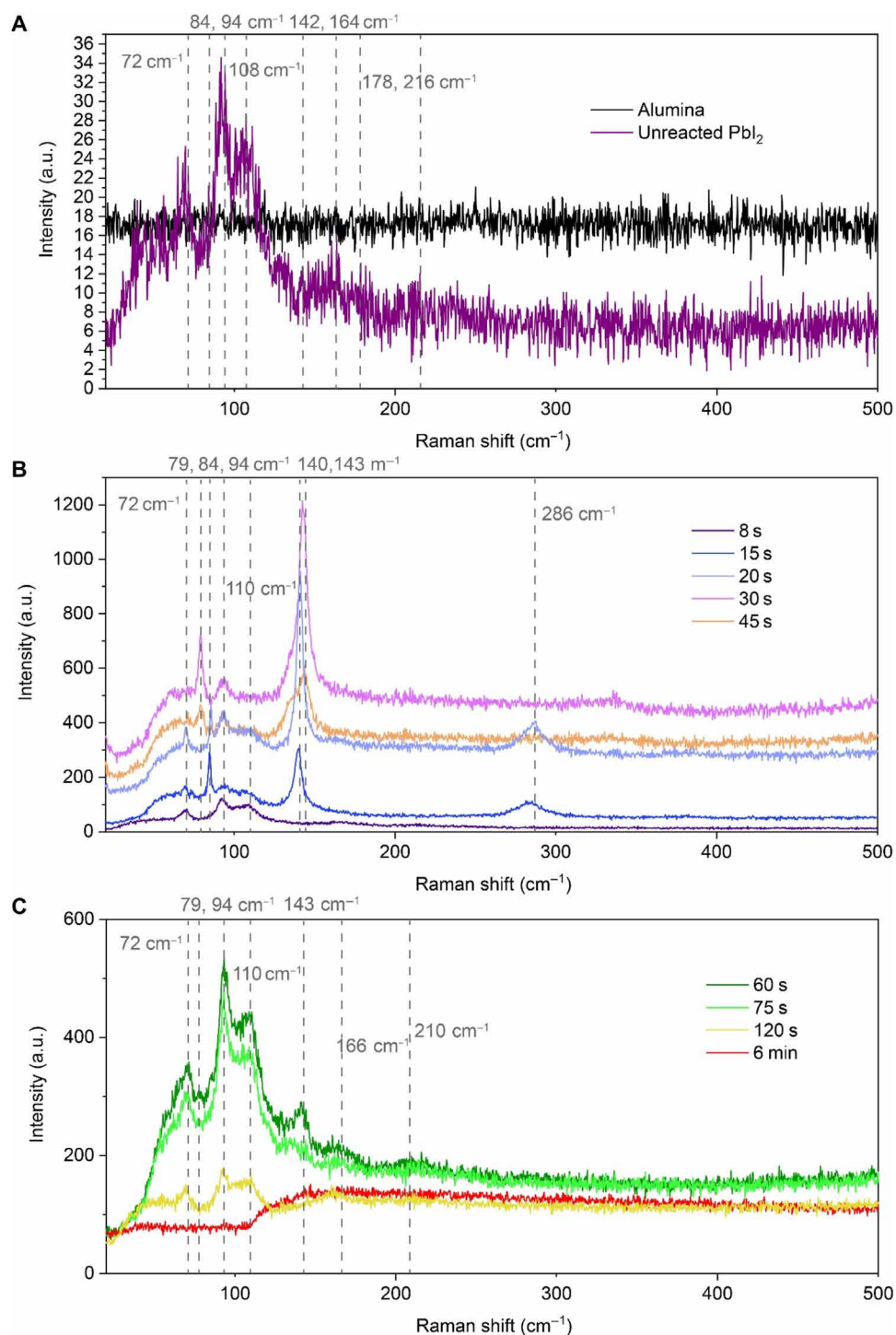


**Fig. 1. Raman spectra monitoring the progress of  $\text{MAPbI}_3$  formation in the sequential deposition reaction.** (A) Control measurements of the alumina scaffold on glass substrate and the unreacted  $\text{PbI}_2$  film. (B) Samples reacted in MAI solution (5 mg/ml) after 8, 15, 20, 30, and 45 s. (C) Samples reacted in MAI solution (5 mg/ml) after 60, 75, and 120 s and 6 min. a.u., arbitrary units.

progresses, the peak becomes less sharp. We further analyzed this process computationally. First, we construct models with different size supercells of  $\text{PbI}_2$  with an increasing number of layers in the (001) direction, depicted in fig. S8. We then compute the XRD spectra of these supercells, shown in fig. S9, and compare them with the

experimental XRD spectra from fig. S7B. We find that, during the initial seconds of the dipping, layers of edge-sharing  $\text{PbI}_6$  octahedra stack over each other in the (001) direction of crystalline  $\text{PbI}_2$ . We attribute this fact to intercalation commencing before the formation of  $\text{MAPbI}_3$ .

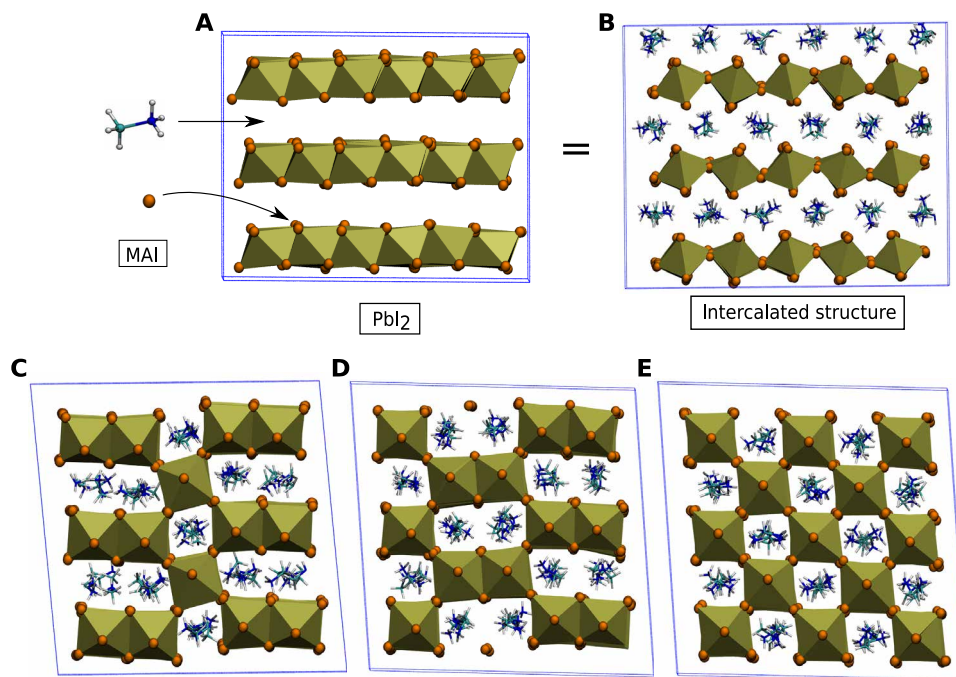


**Fig. 2. Phase transition via intermediate phases.** (A) and (B) show the intercalation process. (B) to (E) display the phase transition from quasi-2D–intercalated structure (B) to perovskite phase of  $\text{MAPbI}_3$  (E).  $\text{Pb-I}$  complexes are shown as golden polyhedra with  $\text{Pb}^{2+}$  in the center and  $\text{I}^-$  as dark orange balls on the corners.  $\text{MA}^+$  cations are shown with balls and sticks with carbon as light blue, nitrogen as dark blue, and hydrogens being white. Similar structures have been observed for other materials such as  $\text{MgSiO}_3$ ,  $\text{CsIrO}_3$ ,  $\text{AgTaS}_3$ ,  $\text{NaMgF}_3$ ,  $\text{MgGeO}_3$ , and  $\text{UFeS}_3$  (28).

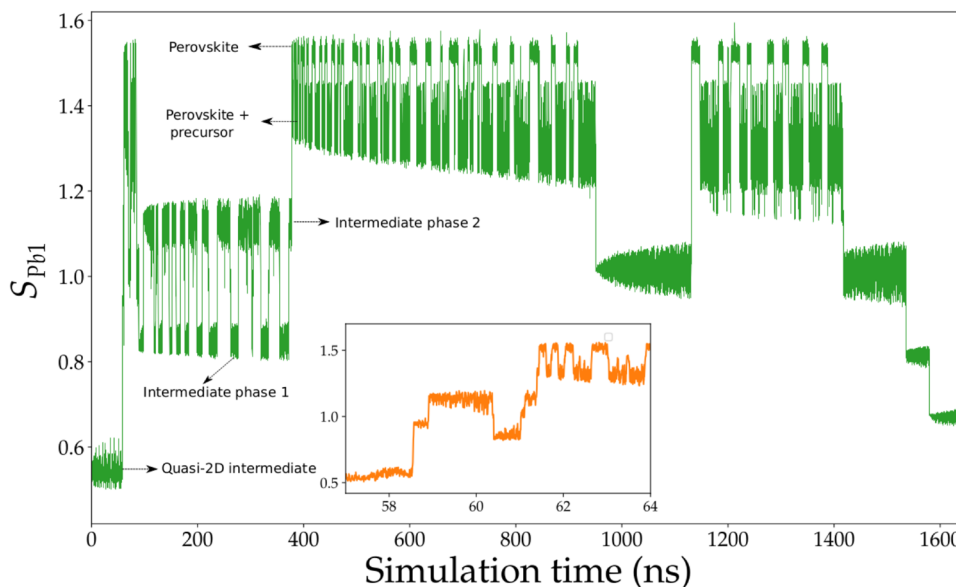


**Fig. 3. Structure factor.** Evolution of first peak of structure factor of  $\text{Pb}^{2+}$  ions ( $S_{\text{Pb1}}$ ) with WTMetaD simulation at 370 K. Inset is a zoom of  $S_{\text{Pb1}}$  for the first transition from quasi-2D to 3D.

We further examine our simulations by performing in situ grazing incidence wide-angle x-ray scattering (GIWAXS) experiments (37) on sequential deposition; see Methods for details. We highlight the fact that these experiments are performed at room temperature. Figure 4A shows the GIWAXS data from the pure  $\text{PbI}_2$  layer. Figure 4 (B and C) shows such a film during the two-step conversion to  $\text{MAPbI}_3$  (Fig. 4B) and  $\text{FAPbI}_3$  (Fig. 4C) after  $\sim 5$  s of application of

the solvent. At the beginning of the reaction, we find, in both samples, a very broad feature at  $q \sim 0.6$  to  $0.9 \text{ \AA}^{-1}$  (broken cyan), which could be assigned to a disordered intercalated phase. This can be also explained with the above-discussed calculations of layered calculations. As the reaction proceeds, we observe the partial conversion of  $\text{PbI}_2$  to the respective perovskite structures; see the presence of Bragg reflection of  $\alpha$ - $\text{FAPbI}_3$  (Fig. 4C) at room temperature. This

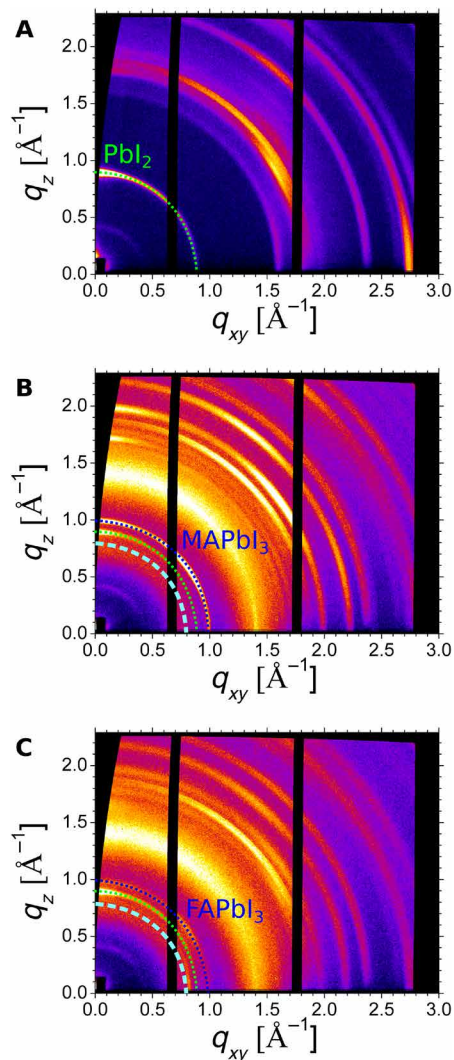


**Fig. 4. GIWAXS spectra.** (A) is pure  $\text{PbI}_2$ , (B) is during conversion to  $\text{MAPbI}_3$  (after 5 s), and (C) is during transformation to  $\text{FAPbI}_3$  (after 5 s). In (B) and (C), both pure  $\text{PbI}_2$  and the  $\text{MAPbI}_3$  and  $\text{FAPbI}_3$  scattering features are marked by dotted lines. An additional broad feature is at  $q \sim 0.6$  to  $0.9 \text{ \AA}^{-1}$  (broken cyan).

provides substantial proof for our simulation results. We take an additional step and directly perform thin-film experiments at room temperature. First, we deposit a layer of  $\text{PbI}_2$  and directly dip it in FAI solution; see movie S5. XRD measurements on this film (fig. S10) show that  $\text{PbI}_2$  is partially converted to  $\alpha\text{-FAPbI}_3$ . We expect this from insufficient diffusion of large  $\text{FA}^+$  cations in a highly compact  $\text{PbI}_2$  film. We design a computational experiment to explain this observation. We remove parts of FAI from the FAI-intercalated  $\text{PbI}_2$  and perform DFT-based variable cell enthalpic relaxation of this structure. We observe that FAI-removed pieces of intercalated structure turn into face-sharing Pb-I octahedra, thus forming characteristic motives of the  $\delta\text{-FAPbI}_3$ . We depict this whole process in fig. S11.

We further scrutinize our simulations and compare the orientational changes in the metadynamics trajectory with in situ GIWAXS data. During the initial stage of the phase transition from  $\text{PbI}_2$  to perovskite structure, GIWAXS experimental results presented in

Fig. 4 and fig. S12 (38) show that the first perovskite Bragg reflection (001 in cubic notation, 002/110 in tetragonal notation) is oriented at a polar angle of  $\sim 35^\circ$ , defining  $0^\circ$  as the horizontal plane direction of 001- $\text{PbI}_2$ . This orientation corresponds to the 111 plane (cubic notation) being parallel to the substrate plane. Similar to these experiments, we calculate the initial orientation of perovskite structure in our simulations. We take  $0^\circ$  as the horizontal plane direction of the 001- $\text{PbI}_2$ -intercalated structure. We find a similar tilt of  $\sim 35^\circ$  of the 001 plane. A pictorial representation of this whole process is shown in figs. S13 and S14. We conclude that our simulations are consistent with experimental observations, because the orientational changes of the structure during the crystallization are well reproduced.

### Thin-film experiments on formation of phase-pure $\alpha\text{-FAPbI}_3$

In this section, we aim to use the above-presented insights to make phase-pure thin films of  $\alpha\text{-FAPbI}_3$ . On the basis of the intercalation of monovalent cations, we expect that the formation of  $\text{FAPbI}_3$  would strongly depend on the microstructure of initially deposited  $\text{PbI}_2$  thin films. To understand this effect, we design three different experiments with tailored crystallinity and porosity of  $\text{PbI}_2$ . Experimental details are provided in Methods. Figure 5 (A to C) shows the scanning electron microscopy (SEM) images of the three  $\text{PbI}_2$  films, showing the top-view surface morphologies. The porosity of these films is in an increasing order from first to third. From Fig. 5C, one can see that the third film is highly porous compared to the others. Next, we use only FAI and perform an identical sequential deposition procedure for their conversion to  $\text{FAPbI}_3$ ; see experimental details in Methods. Figure 5 (D to F) shows the XRD patterns of the final  $\text{FAPbI}_3$  films. We observe the formation of cubic( $\alpha$ ) phase of  $\text{FAPbI}_3$  in all cases. However, we find that the substantial amounts of unconverted  $\text{PbI}_2$  are present in the first two cases (Fig. 5, D and E), whereas conversion to  $\text{FAPbI}_3$  from a highly porous film (the third case) does not contain any detectable amount of  $\text{PbI}_2$  and  $\delta\text{-FAPbI}_3$ , evident from Fig. 5F. From these experiments, we conclude that a highly porous thin film of  $\text{PbI}_2$  leads to the formation of a kinetically stable (see fig. S15) phase-pure  $\alpha\text{-FAPbI}_3$ .

### DISCUSSION

We point out that the phase transition from a quasi-2D to 3D perovskite structure via rotation of  $\text{PbI}_6$  octahedra is a general pathway to form the perovskite structure. This theoretical result can be useful as such a quasi-2D phase can be tailored with additives to synthesize high-quality and stable  $\alpha\text{-FAPbI}_3$ . One example is anion additives such as chloride, which is widely known to modify the crystallization process and has become a commonly used additive to make high efficiency  $\alpha\text{-FAPbI}_3$ -based solar cells. Recent XRD (39) and cryo-electron microscopy (40) experiments have shown that chloride induces a quasi-2D-like intermediate phase that can help in the nucleation of  $\alpha\text{-FAPbI}_3$ . Therefore, the current theoretical approach presented here can be applied to unravel the effects of different additives. Moreover, the reverse phase transition from 3D to quasi-2D might also be present during degradation leading to  $\text{PbI}_2$ .

### Conclusions

By using WTMetaD, we explore the phase transition paths in the two-step deposition of halide perovskites. Combining simulations and experiments, we reveal the intricate details of the phase

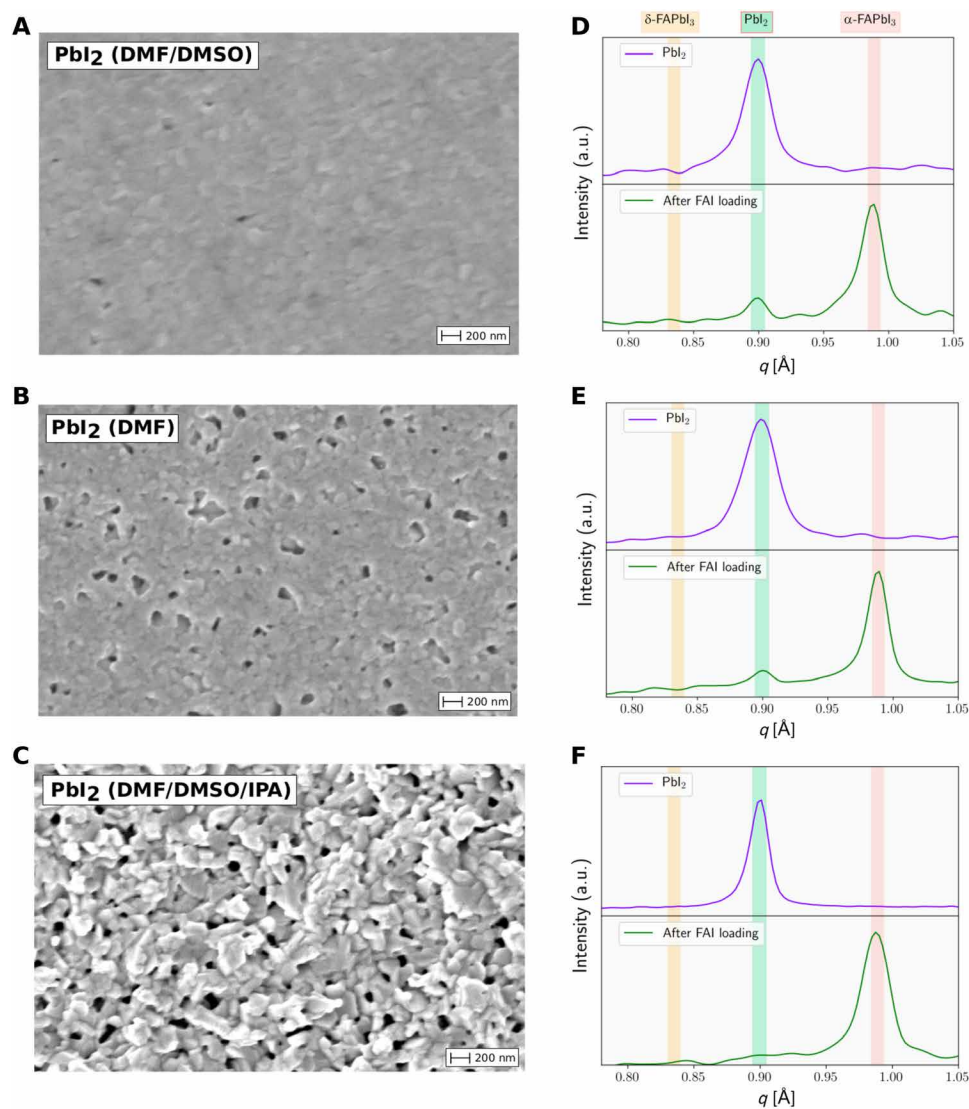


**Fig. 5. Thin-film experiments of sequential deposition of FAPbI<sub>3</sub>.** (A) to (C) are the SEM images showing the surface topography, and (D) to (F) are the corresponding XRD spectra of thin films before and after conversion to FAPbI<sub>3</sub>.

transition of MAPbI<sub>3</sub> and FAPbI<sub>3</sub>. We find a low-temperature crystallization pathway for the  $\alpha$ -FAPbI<sub>3</sub>. Our combined experimental and simulation study will help in designing better industrial-scale processing techniques for MAPbI<sub>3</sub> and FAPbI<sub>3</sub>. In the end, we point out that other Raman studies (30, 41) have also demonstrated the PbI<sub>2</sub> intercalation with other organic molecules such as ammonia, ethylamine (C<sub>2</sub>H<sub>5</sub>NH<sub>2</sub>), butylamine (C<sub>4</sub>H<sub>9</sub>NH<sub>2</sub>), and even larger ones such as cyclohexenyl ethyl ammonium (C<sub>6</sub>H<sub>9</sub>C<sub>2</sub>H<sub>4</sub>NH<sub>3</sub><sup>+</sup>). Therefore, our combined experimental and simulations study can be extended to study the formation of other systems such as lower-dimensional (2D) perovskites as well.

## METHODS

We use a fixed point charge model for MAPbI<sub>3</sub> (42) with a 1.0-nm cutoff for nonbonded interactions. We take the PbI<sub>2</sub> parameters from this force field and prepare the force fields for FAPbI<sub>3</sub> by mixing rules. In variable cell isothermal-isobaric simulations, this force field gives

stable hexagonal ( $\delta$ ) and cubic ( $\alpha$ ) and can also reproduce all other experimentally known 4H and 6H polytypes of FAPbI<sub>3</sub>. Electrostatics are treated with the particle-particle particle-mesh Ewald method, and the SHAKE algorithm (43) is used to constrain covalent bonds to hydrogen. All systems are simulated with the Large-scale Atomic/Molecular Massively Parallel Simulator code (31 March 2017) (44). We first minimize all systems with a conjugate gradient algorithm, keeping a tolerance of maximum force of 10<sup>-3</sup> kcal/molÅ. After minimization, we perform a 100-ps NVT equilibration run. All production run simulations presented in this work were carried out in the isothermal-isobaric ensemble with a velocity rescaling thermostat (45) of 0.1-ps relaxation time and a Parrinello-Rahman barostat (46). All WTMetaD simulations are performed with PLUMED 2.4 (47).

## DFT calculations

We use Quantum ESPRESSO (48) for geometry optimization with a generalized gradient approximation to Kohn-Sham DFT, namely, the Perdew-Burke-Ernzerhof functional (49) with Grimme D3 (50)

dispersion corrections for van der Waals interactions. In all DFT calculations, we use ultrasoft pseudo-potentials with a plane wave basis set of 60-Rydberg (Ry) kinetic energy cutoff for the wave functions and a 480-Ry density cutoff. All structure files are reported in the Supplementary Materials. To estimate the energy barrier between  $\delta$ -FAPbI<sub>3</sub> and  $\alpha$ -FAPbI<sub>3</sub>, we first explore a path between these two phases by performing classical MD simulations at different temperatures and pressures. An atomistic movie of this phase transition is shown in movie S6. For estimating the energy barrier, we perform DFT calculations along the path shown in movie S6 and fig. S15.

### Collective variables

In this study, we use an experimentally measurable quantity, the structure factor (51) as a collective variable (CV). In particular, we use the Debye form (52) of structure factor [ $S(q)$ ]

$$S(q) = 1 + \frac{1}{N} \sum_{i=1}^N \sum_{j \neq i}^N \frac{\sin(qr_{ij})}{qr_{ij}} \quad (1)$$

In this equation, the sum is done over neighbors of atom  $i$ , which are contained in a sphere of radius  $r_c$ . As previously done, we have added a damping function to remove the termination effects from a finite cutoff. Further details are provided in (51). Contrary to previous applications, perovskites are multicomponent systems. To deal with this, we use a linear combination of the first two peaks of the structure factors of individual species Pb<sup>2+</sup> and MA<sup>+</sup>, as shown in fig. S16. We design this CV on the basis of two main factors: (i) Pb<sup>2+</sup> are the heaviest atoms and contribute most to XRD spectra; and (ii) our previous simulations (53) have revealed that the monovalent cations (MA<sup>+</sup> and FA<sup>+</sup>) play an important role in the crystallization process of halide perovskite. Furthermore, these are also the peaks that are assigned to identify perovskite formation in GIWAXS experiments; see Fig. 4. We represent the MA<sup>+</sup> and FA<sup>+</sup> cations with the center of C–N bond similar to our previous study (53)

$$CV = S_{Pb1} + S_{Pb2} + S_{MA1} + S_{MA2} \quad (2)$$

We use this CV to perform the phase transition from the quasi-2D phase to 3D perovskite. In this study, we have focused on the phase transition of halide perovskites. A similar methodology can also be used to study the phase transitions in many other perovskites systems such as MgSiO<sub>3</sub> (54), which is important for earth seismic activities and perovskite solid electrolytes that are promising materials for next-generation Li<sup>+</sup> ion solid-state batteries (55).

### In situ GIWAXS experiments

X-ray scattering experiments were done at beamline ID10 of the European Synchrotron Radiation Facility with a photon energy of 22 keV under nitrogen atmosphere. The beam size was 20  $\mu$ m in vertical direction and 120  $\mu$ m in horizontal direction. GIWAXS data were measured with a PILATUS 300K (487  $\times$  619 pixels; pixel size: 0.172 mm) with a sample detector distance of 472 mm under an angle of incidence of 0.14°. Integration times for each image were 2 s. All images were transformed from angular space to q-space and corrected for refraction effects.

### FAPbI<sub>3</sub> thin-film experiments

#### Substrate preparation

Fluorine-doped tin oxide (FTO) glass substrates (TCO glass, NSG 10, Nippon sheet glass, Japan) were cleaned by ultrasonication in

Hellmanex (2%, deionized water), rinsed thoroughly with deionized water and ethanol, and then treated in oxygen plasma for 15 min. A 30-nm blocking layer (TiO<sub>2</sub>) was deposited on the cleaned FTO by spray pyrolysis at 450°C using a commercial titanium diisopropoxide bis(acetylacetonate) solution (75% in 2-propanol; Sigma-Aldrich) diluted in anhydrous ethanol (1:9 volume ratio) as a precursor and oxygen as a carrier gas. A mesoporous TiO<sub>2</sub> layer was deposited by spin-coating a diluted paste in ethanol (1:8.5 weight ratio) (Dyesol 30NRD:ethanol) (3000 rpm; acceleration, 2000 rpm for 20 s) onto the substrate containing a TiO<sub>2</sub> compact layer and then sintered at 450°C for 30 min in dry air.

#### Fabrication of perovskite films

Two stock solutions of 1.15 M PbI<sub>2</sub> were dissolved in 1 ml of *N,N'*-dimethylformamide (DMF) and DMF/dimethyl sulfoxide (DMSO) (1 ml of DMF and 100  $\mu$ l of DMSO), respectively, and then stirred at 70°C for 12 hours. Next, these solutions were spin-coated on FTO/c-TiO<sub>2</sub>/meso-TiO<sub>2</sub> substrate at 4000 rpm for 45 s and then heated at 80°C for 3 to 5 min to remove the solvents. After cooling down, the FAI (60 mg) dissolved in 1 ml of isopropyl alcohol (IPA) was spin-coated on top of the PbI<sub>2</sub> whether the one dissolved in DMF or DMF/DMSO at 2500 rpm for 45 s followed by annealing at 80°C for 40 min. In case of the effect of DMF/DMSO with IPA, first, after cooling down the substrate (PbI<sub>2</sub> dissolved in DMF/DMSO), IPA solution was held on the substrate for 1 min without any further post-annealing, and after that, the film was spin-coated at 4000 rpm for 45 s (56, 57). Next, the FAI was spin-coated at 2500 rpm for 45 s followed by annealing at 80°C for 40 min.

#### Dipping experiments on FAPbI<sub>3</sub>

For FAPbI<sub>3</sub> samples, 1.3 M PbI<sub>2</sub> solution (DMF:DMSO = 9:1) was spin-coated at a speed of 2000 rpm/min for 30 s. Then, the PbI<sub>2</sub> layer was annealed at 70°C for 1 min. After that, the PbI<sub>2</sub> layer was dipped inside an IPA solution of FAI (20 mg/ml).

#### Experiments on MAPbI<sub>3</sub>

MAPbI<sub>3</sub> samples were prepared first by depositing a PbI<sub>2</sub> layer directly on glass substrates for the XRD measurements. Samples used for the Raman spectroscopy were made on glass with a mesoporous layer of 23-nm particles of alumina on them. A 1.3 M PbI<sub>2</sub> solution in DMF was spin-coated, and the film was then heated at 70°C for 10 min. This was followed by the reaction with 5 mg/ml MAI in IPA at room temperature, where the sample was dipped in the solution for different periods of time. The final steps were washing in pure IPA to halt the reaction and heating at 70°C for 10 min.

#### XRD measurements

XRD data are measured in the Bragg-Brentano geometry using a Bruker D8 Advance powder x-ray diffractometer. The setup has Cu K $\alpha$  ( $\lambda = 1.54 \text{ \AA}$ ) radiation and operates in reflection, theta-theta mode (fixed sample) with a 2D strip detector. A beam mask of 1 cm was chosen to suitably irradiate the films being measured. A step size of 0.01° was used for measurement, and time per step was 0.15 s. XRD spectra for MAPbI<sub>3</sub> are shown in fig. S7 and that for FAPbI<sub>3</sub> are presented in fig. S10.

#### Raman spectroscopy

Raman spectroscopy was conducted on a HORIBA LabRAM HR Raman spectrometer. A 532-nm green laser was used for excitation. The focal spot size was about 10  $\mu$ m using a 50 $\times$  long working-distance objective. Previous reports (58) have demonstrated the degradation of the perovskite into PbI<sub>2</sub> under high laser intensities.

A neutral density filter (optical density, 3.0) was used to attenuate the laser intensity to avoid damage to the sample.

Raman spectra were collected for monitoring the progress of MAPbI<sub>3</sub> formation in the sequential deposition reaction. Figure 1A shows spectra for control samples of the alumina scaffold on the glass substrate and an unreacted PbI<sub>2</sub> film. Figure 1B shows spectra for samples that reacted in MAI solution (5 mg/ml) for 8, 15, 20, 30, and 45 s, while Fig. 1C shows those for samples reacted for 60, 75, and 120 s and 6 min.

Figure 1A shows that the control measurement on the substrate shows no peaks in the range of interest, so its contribution to the Raman signal in the rest of the measurements can be neglected under similar measurement conditions. The 2H polytype of PbI<sub>2</sub> has only three atoms in each unit cell, giving rise to 9° of vibrational motion. The spectrum for the unreacted PbI<sub>2</sub> sample shows that peaks at 72 cm<sup>-1</sup> (a doubly degenerate E<sub>g</sub> band) and 94 cm<sup>-1</sup> (a symmetric stretch A<sub>1g</sub>) due to the shearing motion of two iodine layers are present as expected. Additional peaks expected for PbI<sub>2</sub> nanoparticles are detected at 84 and 108 cm<sup>-1</sup>. Peaks that are double in energy of 72, 84, 94, and 108 cm<sup>-1</sup> absorptions are also observed at 142, 164, 178, and 216 cm<sup>-1</sup> and attributed to the overtones of the fundamentals (59).

Now, we discuss the Raman spectra of samples reacted with MAI. These samples are first expected to show indications of the intercalation of the methylammonium ion into the PbI<sub>2</sub> lattice as discussed in the XRD results, followed by structural reorganization to form the perovskite. In the Raman spectra for the hybrid perovskite of interest, because of the considerable difference in mass between the organic and inorganic constituents, the spectral features at different energies are associated with different dynamic processes in the perovskite lattice. The features observed at energies below 200 cm<sup>-1</sup> are ascribed to a combination of Pb-I cage modes and the associated coupled motion of the MA<sup>+</sup> ions. Those signals above 200 cm<sup>-1</sup> are assigned to the molecular vibrations of the cations (27). However, in the data shown in Fig. 1C, for a sample reacted for 6 min, consisting of fully reacted perovskite in the tetragonal phase, very few features are distinguishable as anticipated at room temperature (27). Nevertheless, the dataset consisting of the remaining samples shows interesting changes, particularly at energies below 200 cm<sup>-1</sup>, as the formation of perovskite progresses.

Figure 1B shows the intensification of the peak at 79 cm<sup>-1</sup> corresponding to the perturbed asymmetric breathing mode of a (MAPbI<sub>3</sub>)<sub>4</sub> cluster with reaction time (20). It also shows a sharp peak at 84 cm<sup>-1</sup> at 30 s, which weakens at 45 s, while the peak at 94 cm<sup>-1</sup> strengthens as the reaction progresses beyond this point. From DFT calculations reported in the literature (20), the former can be assigned to the symmetric breathing mode of the PbI<sub>6</sub> octahedra and the latter to the perturbed symmetric breathing mode of a (MAPbI<sub>3</sub>)<sub>4</sub> cluster. These peaks, particularly the Pb-I breathing mode at 94 cm<sup>-1</sup>, vanish as the perovskite formation reaction progresses (Fig. 1C; see data for 75 and 120 s and 6 min).

## SUPPLEMENTARY MATERIALS

Supplementary material for this article is available at <http://advances.sciencemag.org/cgi/content/full/7/17/eabe3326/DC1>

## REFERENCES AND NOTES

- A. Kojima, K. Teshima, Y. Shirai, T. Miyasaka, Organometal halide perovskites as visible-light sensitizers for photovoltaic cells. *J. Am. Chem. Soc.* **131**, 6050–6051 (2009).
- J. Burschka, N. Pellet, S.-J. Moon, R. Humphry-Baker, P. Gao, M. K. Nazeeruddin, M. Grätzel, Sequential deposition as a route to high-performance perovskite-sensitized solar cells. *Nature* **499**, 316–319 (2013).
- Q. Jiang, Y. Zhao, X. Zhang, X. Yang, Y. Chen, Z. Chu, Q. Ye, X. Li, Z. Yin, J. You, Surface passivation of perovskite film for efficient solar cells. *Nat. Photonics* **13**, 460–466 (2019).
- W. S. Yang, B.-W. Park, E. H. Jung, N. J. Jeon, Y. C. Kim, D. U. Lee, S. S. Shin, J. Seo, E. K. Kim, J. H. Noh, S. I. Seok, Iodide management in formamidinium-lead-halide-based perovskite layers for efficient solar cells. *Science* **356**, 1376–1379 (2017).
- K. Liang, D. B. Mitzi, M. T. Prikas, Synthesis and characterization of organic–inorganic perovskite thin films prepared using a versatile two-step dipping technique. *Chem. Mater.* **10**, 403–411 (1998).
- S. Razza, F. Di Giacomo, F. Matteocci, L. Cinà, A. L. Palma, S. Casaluci, P. Cameron, A. D'Epifanio, S. Licocchia, A. Reale, T. M. Brown, A. Di Carlo, Perovskite solar cells and large area modules (100 cm<sup>2</sup>) based on an air flow-assisted PbI<sub>2</sub> blade coating deposition process. *J. Power Sources* **277**, 286–291 (2015).
- P. Li, C. Liang, B. Bao, Y. Li, X. Hu, Y. Wang, Y. Zhang, F. Li, G. Shao, Y. Song, Inkjet manipulated homogeneous large size perovskite grains for efficient and large-area perovskite solar cells. *Nano Energy* **46**, 203–211 (2018).
- N.-G. Park, K. Zhu, Scalable fabrication and coating methods for perovskite solar cells and solar modules. *Nat. Rev. Mater.* **5**, 333–350 (2020).
- H. Minemawari, T. Yamada, H. Matsui, J. Tsutsumi, S. Haas, R. Chiba, R. Kumai, T. Hasegawa, Inkjet printing of single-crystal films. *Nature* **475**, 364–367 (2011).
- D. Bi, C. Yi, J. Luo, J.-D. Décoppet, F. Zhang, S. M. Zakeeruddin, X. Li, A. Hagfeldt, M. Grätzel, Polymer-templated nucleation and crystal growth of perovskite films for solar cells with efficiency greater than 21%. *Nat. Energy* **1**, 16142 (2016).
- T. M. Brenner, Y. Rakita, Y. Orr, E. Klein, I. Feldman, M. Elbaum, D. Cahen, G. Hodes, Conversion of single crystalline PbI<sub>2</sub> to CH<sub>3</sub>NH<sub>3</sub>PbI<sub>3</sub>: Structural relations and transformation dynamics. *Chem. Mater.* **28**, 6501–6510 (2016).
- Y. Guo, K. Shoyama, W. Sato, Y. Matsuo, K. Inoue, K. Harano, C. Liu, H. Tanaka, E. Nakamura, Chemical pathways connecting lead(II) iodide and perovskite via polymeric plumbate(II) fiber. *J. Am. Chem. Soc.* **137**, 15907–15914 (2015).
- J. B. Patel, R. L. Milot, A. D. Wright, L. M. Herz, M. B. Johnston, Formation dynamics of CH<sub>3</sub>NH<sub>3</sub>PbI<sub>3</sub> perovskite following two-step layer deposition. *J. Phys. Chem. Lett.* **7**, 96–102 (2016).
- D. Barrit, P. Cheng, M.-C. Tang, K. Wang, H. Dang, D.-M. Smilgies, S. Liu, T. D. Anthopoulos, K. Zhao, A. Amassian, Impact of the solvation state of lead iodide on its two-step conversion to MAPbI<sub>3</sub>: An in situ investigation. *Adv. Funct. Mater.* **29**, 1807544 (2019).
- A. W. Sanches, M. A. T. Da Silva, N. J. A. Cordeiro, A. Urbano, S. A. Lourenço, Effect of intermediate phases on the optical properties of PbI<sub>2</sub>-rich CH<sub>3</sub>NH<sub>3</sub>PbI<sub>3</sub> organic–inorganic hybrid perovskite. *Phys. Chem. Chem. Phys.* **21**, 5253–5261 (2019).
- J. Liu, Y. Shirai, X. Yang, Y. Yue, W. Chen, Y. Wu, A. Islam, L. Han, High-quality mixed-organic-cation perovskites from a phase-pure non-stoichiometric intermediate (FAI)<sub>1-x</sub>PbI<sub>2</sub> for solar cells. *Adv. Mater.* **27**, 4918–4923 (2015).
- X. Xu, C. Ma, Y.-M. Xie, Y. Cheng, Y. Tian, M. Li, Y. Ma, C.-S. Lee, S.-W. Tsang, Air-processed mixed-cation Cs<sub>0.15</sub>FA<sub>0.85</sub>PbI<sub>3</sub> planar perovskite solar cells derived from a PbI<sub>2</sub>-CsI-FAI intermediate complex. *J. Mater. Chem. A* **6**, 7731–7740 (2018).
- S. Sanchez, U. Steiner, X. Hua, Phase evolution during perovskite formation—insight from pair distribution function analysis. *Chem. Mater.* **31**, 3498–3506 (2019).
- K. Pradeesh, J. J. Baumberg, G. V. Prakash, In situ intercalation strategies for device-quality hybrid inorganic-organic self-assembled quantum wells. *Appl. Phys. Lett.* **95**, 033309 (2009).
- S. M. Jain, B. Philippe, E. M. J. Johansson, B.-W. Park, H. Rensmo, T. Edvinsson, G. Boschloo, Vapor phase conversion of PbI<sub>2</sub> to CH<sub>3</sub>NH<sub>3</sub>PbI<sub>3</sub>: Spectroscopic evidence for formation of an intermediate phase. *J. Mater. Chem. A* **4**, 2630–2642 (2016).
- A. Laio, M. Parrinello, Escaping free-energy minima. *Proc. Natl. Acad. Sci. U.S.A.* **99**, 12562–12566 (2002).
- C.-J. Que, C.-J. Mo, Z.-Q. Li, G.-L. Zhang, Q.-Y. Zhu, J. Dai, Perovskite-like organic–inorganic hybrid lead iodide with a large organic cation incorporated within the layers. *Inorg. Chem.* **56**, 2467–2472 (2017).
- M. E. Kamminga, G. A. de Wijs, R. W. A. Havenith, G. R. Blake, T. T. M. Palstra, The role of connectivity on electronic properties of lead iodide perovskite-derived compounds. *Inorg. Chem.* **56**, 8408–8414 (2017).
- C. Lermer, A. Senocrate, I. Moudrakovski, T. Seewald, A.-K. Hatz, P. Mayer, F. Pielhofer, J. A. Jaser, L. Schmidt-Mende, J. Maier, B. V. Lotsch, Completing the picture of 2-(aminomethylpyridinium) lead hybrid perovskites: Insights into structure, conductivity behavior, and optical properties. *Chem. Mater.* **30**, 6289–6297 (2018).
- C. C. Stoumpos, L. Mao, C. D. Malliakas, M. G. Kanatzidis, Structure–band gap relationships in hexagonal polytypes and low-dimensional structures of hybrid tin iodide perovskites. *Inorg. Chem.* **56**, 56–73 (2017).
- P. Gratia, I. Zimmermann, P. Schouwink, J. H. Yum, J.-N. Audinot, K. Sivula, T. Wirtz, M. K. Nazeeruddin, The many faces of mixed ion perovskites: Unraveling and understanding the crystallization process. *ACS Energy Lett.* **2**, 2686–2693 (2017).

27. A. M. A. Leguy, A. R. Goñi, J. M. Frost, J. Skelton, F. Brivio, X. Rodríguez-Martínez, O. J. Weber, A. Pallipurath, M. I. Alonso, M. Campoy-Quiles, M. T. Weller, J. Nelson, A. Walsh, P. R. F. Barnes, Dynamic disorder, phonon lifetimes, and the assignment of modes to the vibrational spectra of methylammonium lead halide perovskites. *Phys. Chem. Chem. Phys.* **18**, 27051–27066 (2016).
28. H. Noël, J. Padiou, Structure cristalline de FeUS<sub>3</sub>. *Acta Cryst. Sec. B* **32**, 1593–1595 (1976).
29. M. Daub, H. Hillebrecht, Tailoring the band gap in 3D hybrid perovskites by substitution of the organic cations: (CH<sub>3</sub>NH<sub>3</sub>)<sub>1–2y</sub>(NH<sub>3</sub>(CH<sub>2</sub>)<sub>2</sub>NH<sub>3</sub>)<sub>2y</sub>Pb<sub>1–y</sub>I<sub>3</sub> (0 ≤ y ≤ 0.25). *Chem. A Eur. J.* **24**, 9075–9082 (2018).
30. R. F. Warren, W. Y. Liang, Raman spectroscopy of new lead iodide intercalation compounds. *J. Phys. Condens. Matter* **5**, 6407 (1993).
31. G. Pellegrino, S. D'Angelo, I. Deretzis, G. G. Condorelli, E. Smecca, G. Malandrino, A. L. Magna, A. Alberti, From PbI<sub>2</sub> to MAPbI<sub>3</sub> through layered intermediates. *J. Phys. Chem. C* **120**, 19768–19777 (2016).
32. P. A. Beckmann, A review of polytypism in lead iodide. *Crystal Research and Technology* **45**, 455–460 (2010).
33. M. Y. Khilji, W. F. Sherman, G. R. Wilkinson, Raman study of three polytypes of PbI<sub>2</sub>. *J. Raman Spectrosc.* **13**, 127–133 (1982).
34. A. Ummadisingu, M. Grätzel, Revealing the detailed path of sequential deposition for metal halide perovskite formation. *Sci. Adv.* **4**, e1701402 (2018).
35. A. Ummadisingu, L. Steier, J.-Y. Seo, T. Matsui, A. Abate, W. Tress, M. Grätzel, The effect of illumination on the formation of metal halide perovskite films. *Nature* **545**, 208–212 (2017).
36. H. A. Harms, N. Tétréault, N. Pellet, M. Bensimon, M. Grätzel, Mesoscopic photosystems for solar light harvesting and conversion: Facile and reversible transformation of metal-halide perovskites. *Faraday Discuss.* **176**, 251–269 (2015).
37. A. Greco, A. Hinderhofer, M. I. Dar, N. Arora, J. Hagenlocher, A. Chumakov, M. Grätzel, F. Schreiber, Kinetics of ion-exchange reactions in hybrid organic–inorganic perovskite thin films studied by in situ real-time x-ray scattering. *J. Phys. Chem. Lett.* **9**, 6750–6754 (2018).
38. T. Miyadera, Y. Shibata, T. Koganezawa, T. N. Murakami, T. Sugita, N. Tanigaki, M. Chikamatsu, Crystallization dynamics of organolead halide perovskite by real-time x-ray diffraction. *Nano Lett.* **15**, 5630–5634 (2015).
39. T. Zhang, Q. Xu, F. Xu, Y. Fu, Y. Wang, Y. Yan, L. Zhang, Y. Zhao, Spontaneous low-temperature crystallization of α-FAPbI<sub>3</sub> for highly efficient perovskite solar cells. *Sci. Bull.* **64**, 1608–1616 (2019).
40. N. S. Dutta, N. K. Noel, C. B. Arnold, Crystalline nature of colloids in methylammonium lead halide perovskite precursor inks revealed by cryo-electron microscopy. *J. Phys. Chem. Lett.* **11**, 5980–5986 (2020).
41. C. C. Coleman, B. Magness, P. Melo, H. Goldwhite, W. Tikkanen, Q. Tham, K. Pham, R. Jacubinas, R. B. Kaner, R. E. Treece, Intercalation of hydrazines in lead iodide. *J. Phys. Chem. Solid* **57**, 1153–1158 (1996).
42. C. Caddeo, M. I. Saba, S. Meloni, A. Filippetti, A. Mattoni, Collective molecular mechanisms in the CH<sub>3</sub>NH<sub>3</sub>PbI<sub>3</sub> dissolution by liquid water. *ACS Nano* **11**, 9183–9190 (2017).
43. J.-P. Ryckaert, G. Ciccotti, H. J. Berendsen, Numerical integration of the cartesian equations of motion of a system with constraints: Molecular dynamics of *n*-alkanes. *J. Comput. Phys.* **23**, 327–341 (1977).
44. S. Plimpton, Fast parallel algorithms for short-range molecular dynamics. *J. Comput. Phys.* **117**, 1–19 (1995).
45. G. Bussi, D. Donadio, M. Parrinello, Canonical sampling through velocity rescaling. *J. Chem. Phys.* **126**, 014101 (2007).
46. M. Parrinello, A. Rahman, Polymorphic transitions in single crystals: A new molecular dynamics method. *J. Appl. Phys.* **52**, 7182–7190 (1981).
47. G. A. Tribello, M. Bonomi, D. Branduardi, C. Camilloni, G. Bussi, PLUMED 2: New feathers for an old bird. *Comput. Phys. Commun.* **185**, 604–613 (2014).
48. P. Giannozzi, S. Baroni, N. Bonini, M. Calandra, R. Car, C. Cavazzoni, D. Ceresoli, G. L. Chiarotti, M. Cococcioni, I. Dabo, A. D. Corso, S. de Gironcoli, S. Fabris, G. Fratesi, R. Gebauer, U. Gerstmann, C. Gougousis, A. Kokalj, M. Lazzeri, L. Martin-Samos, N. Marzari, F. Mauri, R. Mazzarello, S. Paolini, A. Pasquarello, L. Paulatto, C. Sbraccia, S. Scandolo, G. Sclauzero, A. P. Seitsonen, A. Smogunov, P. Umari, R. M. Wentzcovitch, QUANTUM ESPRESSO: A modular and open-source software project for quantum simulations of materials. *J. Phys. Condens. Matter* **21**, 395502 (2009).
49. J. P. Perdew, K. Burke, M. Ernzerhof, Generalized gradient approximation made simple. *Phys. Rev. Lett.* **77**, 3865 (1996).
50. S. Grimme, Semiempirical GGA-type density functional constructed with a long-range dispersion correction. *J. Comput. Chem.* **27**, 1787–1799 (2006).
51. H. Niu, P. M. Piaggi, M. Invernizzi, M. Parrinello, Molecular dynamics simulations of liquid silica crystallization. *Proc. Natl. Acad. Sci. U.S.A.* **115**, 5348–5352 (2018).
52. P. Debye, Zerstreuung von Röntgenstrahlen. *Ann. Phys.* **351**, 809–823 (1915).
53. P. Ahlawat, M. I. Dar, P. Piaggi, M. Grätzel, M. Parrinello, U. Rothlisberger, Atomistic mechanism of the nucleation of methylammonium lead iodide perovskite from solution. *Chem. Mater.* **32**, 529–536 (2020).
54. A. R. Oganov, S. Ono, Theoretical and experimental evidence for a post-perovskite phase of MgSiO<sub>3</sub> in Earth's D'' layer. *Nature* **430**, 445–448 (2004).
55. Y. Li, H. Xu, P.-H. Chien, N. Wu, S. Xin, L. Xue, K. Park, Y.-Y. Hu, J. B. Goodenough, A perovskite electrolyte that is stable in moist air for lithium-ion batteries. *Angew. Chem. Int. Ed.* **57**, 8587–8591 (2018).
56. E. A. Alharbi, A. Y. Alyamani, D. J. Kubicki, A. R. Uhl, B. J. Walder, A. Q. Alanazi, J. Luo, A. Burgos-Caminal, A. Albadri, H. Albrithen, M. H. Alotaibi, J.-E. Moser, S. M. Zakeeruddin, F. Giordano, L. Emsley, M. Grätzel, Atomic-level passivation mechanism of ammonium salts enabling highly efficient perovskite solar cells. *Nat. Commun.* **10**, 3008 (2019).
57. E. A. Alharbi, M. I. Dar, N. Arora, M. H. Alotaibi, Y. A. Alzhrani, P. Yadav, W. Tress, A. Alyamani, A. Albadri, S. M. Zakeeruddin, M. Grätzel, Perovskite solar cells yielding reproducible photovoltage of 1.20 V. *Research* **2019**, 8474698 (2019).
58. M. Ledinskyy, P. Löper, B. Niesen, J. Holovsky, S.-J. Moon, J.-H. Yum, S. De Wolf, A. Fejfar, C. Ballif, Raman spectroscopy of organic-inorganic halide perovskites. *J. Phys. Chem. Lett.* **6**, 401–406 (2015).
59. C.-X. Sheng, Y. Zhai, E. Olejnik, C. Zhang, D. Sun, Z. V. Vardeny, Laser action and photoexcitations dynamics in PbI<sub>2</sub> films. *Opt. Mater. Express* **5**, 530–537 (2015).

**Acknowledgments:** P.A. is thankful to D. Mitzi and C. Stoumpos for insightful discussions. We thank the European Synchrotron Radiation Facility for provision of synchrotron radiation, A. Chumakov and O. Konovalov for assistance in using the beamline ID10, and A. Greco for assistance with the GIWAXS analysis. The computational time for this work was provided by the Swiss National Supercomputing Centre (CSCS) and SCITAS supercomputing center at EPFL China. We use “quasi-2D” nomenclatures based on literature of halide perovskites. **Funding:** This research is funded by the Swiss National Science Foundation (SNSF) through the NCCR MUST and individual grant 200020-185092. M.P. acknowledges funding from the European Union grant nos. ERC-2014-AdG-670227/VARMET and NCCR-MARVEL. E.A.A. acknowledges King Abdulaziz City for Science and Technology (KACST) for a fellowship. F.S. thanks the DFG (SPP 2196 and SCHR 700/38-1) for funding. M.I.D. acknowledges funding from a Royal Society University Research Fellowship. A.U. is currently supported by the SNSF through the Postdoc Mobility fellowship (grant no. P400P2\_194439). **Author contributions:** P.A. conceived the research. P.A., M.G., F.S., S.M.Z., U.R., A.H., and M.P. conceptualized the research. P.A. designed and performed all the simulations. A.Hi. and M.I.D. designed and performed the GIWAXS experiments at synchrotron. A.U. designed and performed the ex situ x-ray and Raman experiments on sequential deposition of MAPbI<sub>3</sub>. E.A.A., H.L., and P.A. designed and performed the thin-film experiments on FAPbI<sub>3</sub>. E.A.A. performed the SEM and XRD measurements on FAPbI<sub>3</sub> thin films. H.N. and M.I. contributed to the biased simulations. M.G., F.S., S.M.Z., U.R., A.H., and M.P. guided the research. P.A. and M.P. wrote the first draft. All authors discussed the results and wrote the manuscript. **Competing interests:** A.U. is currently a SNSF fellow at the Cavendish Laboratory, University of Cambridge, UK. M.G. has a part-time affiliation with Max Planck Institute for Solid State Research, Stuttgart, Germany. H.N. is currently affiliated with State Key Laboratory of Solidification Processing, International Center for Materials Discovery, School of Materials Science and Engineering, Northwestern Polytechnical University, Xian 710072, P.R. China. **Data and materials availability:** All data needed to evaluate the conclusions in the paper are present in the paper and/or the Supplementary Materials. Additional data related to this paper may be requested from the authors.

Submitted 19 August 2020

Accepted 5 March 2021

Published 23 April 2021

10.1126/sciadv.abe3326

**Citation:** P. Ahlawat, A. Hinderhofer, E. A. Alharbi, H. Lu, A. Ummadisingu, H. Niu, M. Invernizzi, S. M. Zakeeruddin, M. I. Dar, F. Schreiber, A. Hagfeldt, M. Grätzel, U. Rothlisberger, M. Parrinello, A combined molecular dynamics and experimental study of two-step process enabling low-temperature formation of phase-pure α-FAPbI<sub>3</sub>. *Sci. Adv.* **7**, eabe3326 (2021).

## A combined molecular dynamics and experimental study of two-step process enabling low-temperature formation of phase-pure $\alpha$ -FAPbI<sub>3</sub>

Paramvir Ahlawat, Alexander Hinderhofer, Essa A. Alharbi, Haizhou Lu, Amita Ummadisingu, Haiyang Niu, Michele Invernizzi, Shaik Mohammed Zakeeruddin, M. Ibrahim Dar, Frank Schreiber, Anders Hagfeldt, Michael Grätzel, Ursula Rothlisberger and Michele Parrinello

*Sci Adv* 7 (17), eabe3326.  
DOI: 10.1126/sciadv.abe3326

### ARTICLE TOOLS

<http://advances.sciencemag.org/content/7/17/eabe3326>

### SUPPLEMENTARY MATERIALS

<http://advances.sciencemag.org/content/suppl/2021/04/19/7.17.eabe3326.DC1>

### REFERENCES

This article cites 59 articles, 4 of which you can access for free  
<http://advances.sciencemag.org/content/7/17/eabe3326#BIBL>

### PERMISSIONS

<http://www.sciencemag.org/help/reprints-and-permissions>

Use of this article is subject to the [Terms of Service](#)

---

*Science Advances* (ISSN 2375-2548) is published by the American Association for the Advancement of Science, 1200 New York Avenue NW, Washington, DC 20005. The title *Science Advances* is a registered trademark of AAAS.

Copyright © 2021 The Authors, some rights reserved; exclusive licensee American Association for the Advancement of Science. No claim to original U.S. Government Works. Distributed under a Creative Commons Attribution NonCommercial License 4.0 (CC BY-NC).